PHYSICAL REVIEW B

CONDENSED MATTER

THIRD SERIES, VOLUME 34, NUMBER 7 1 OCTOBER 1986

Photofield-emission spectroscopy of bulk electronic states of tungsten

David Venus
Department of Physics, University of Toronto, Toronto, Ontario, Canada M5S 1A7

Martin J. G. Lee
Department of Physics and Scarborough College, University of Toronto, Toronto, Ontario, Canada M5S 1A7
(Received 5 August 1985; revised manuscript received 24 March 1986)

A novel apparatus for the study of photofield emission has made it possible to observe for what is believed to be the first time departures from free-electron behavior in the total-energy distributions in photofield emission due to transitions between bulk electronic states. For plane-polarized light normally incident on the (100), (110), (111), (211), and (510) crystal planes of tungsten, the distributions are found to depart from free-electron behavior at those energies where there is a rapid variation in the product of the initial and final densities of bulk states along the axis normal to the emission plane. Emission by umklapp processes is also observed. The shapes of the distributions and their polarization dependences are consistent with those expected for nondirect bulk photoexcitation, whereas no clear evidence is found for direct transitions in the bulk. Some possible reasons for this are discussed. It is concluded that photofield emission with light at normal incidence can be used to investigate the spectrum of bulk electronic states between the Fermi level and the vacuum level.

I. INTRODUCTION

Photoemission from a metal, in which an electron is excited by an incident photon and escapes to the vacuum by passing above the surface potential barrier, is well established as a means of studying the electronic states below the Fermi level and above the vacuum level. Two alternative techniques have been proposed to study the electronic states lying between the Fermi level and the vacuum level. The inverse photoelectric effect involves injecting an electron above the vacuum level and measuring the energy of the photon that is emitted when the electron drops to an unoccupied state between the Fermi level and the vacuum level. Photofield emission involves photoexciting an electron from an occupied electronic state below the Fermi level to an unoccupied state between the Fermi level and the vacuum level. A strong static electric field is applied at the surface of the metal so that the photoexcited electron can tunnel through the surface potential barrier to the vacuum, where it is detected and its energy is measured.

Experiments involving the inverse photoelectric effect[1] are difficult to carry out because the cross section for the inverse process is smaller than that for the direct process in the ratio $(q/k)^2 \simeq 10^{-5}$, where q is the wave vector of the photon and k is the wave vector of the electron. Moreover, even with the best instruments currently available, the full width of the resolution function at half maximum height is of the order of 200 meV. Photofield emission involves the direct process, so the emission current is larger and easier to detect. Moreover, by using a monochromatic laser as the source of illumination and a deflection analyzer to determine the energy of the electron in the final state, a resolution function with a full width at half maximum height of the order of 40 meV can readily be achieved. Both techniques yield information about **K**-resolved final states. In inverse photoemission the final state can be selected by adjusting the energy and the angle of incidence of the electron beam. In photofield emission the external current is dominated by final states for which $\mathbf{K}_{\parallel} \simeq 0$ because of the tunneling process. **K**-resolved spectra for different low-index crystal directions can be obtained by measuring emission from the various facets of an approximately hemispherical field emitter.

Among the motivations for the development of photofield emission has been the hope that it will provide a way to measure accurately the spectrum of bulk electronic states between the Fermi level and the vacuum level. However, measurements of the total-energy distribution in photofield emission reported to date[2,3] have not shown the departures from free-electron behavior that are expected to arise from bulk band-structure effects, although some evidence for band-structure effects in photofield emission has been reported,[4,5] and departures from free-electron

behavior in field emission are well established.[6,7] There are two principal reasons for this. The first reason is that previous measurements were made with energy analyzers whose signal-to-noise ratio[8] was inadequate to detect the small variation due to band-structure effects in the exponentially decreasing low-energy tail of the distribution. The second reason is that earlier workers in photofield emission did not select light polarization conditions that are favorable to the observation of the bulk photocurrent. Polarization dependence studies by Venus and Lee[9] have shown that the photocurrent is composed of two components which may be separated by the appropriate choice of the angles of light incidence and linear polarization. The dominant excitation mechanism, surface photoexcitation,[10] occurs when the polarization vector has a component normal to the emitting plane ("*p* polarization"). When the polarization vector is parallel to the emitting plane ("*s* polarization," of which illumination at normal incidence is a special case), surface photoexcitation is extinguished and a much smaller residual photocurrent due to bulk photoexcitation is observed.

This paper reports the first systematic study to our knowledge of departures from free-electron behavior in photofield-emission total-energy distributions using *s*-polarized light. Departures from free-electron behavior were observed on all five of the facets of a tungsten field emitter that were studied. The energies at which the departures occur show a strong correlation with the energies at which band-structure calculations predict a rapid variation in the one-dimensional density of states along the normal to the emitting facet. These results are in agreement with those expected for nondirect photoexcitation in the bulk of the metal. Even though the direct bulk photoeffect is generally much stronger than the nondirect bulk photoeffect, the present series of experiments yielded no clear evidence for direct bulk photoexcitation. Some possible reasons for this are discussed in Sec. IV. It is concluded that photofield emission using *s*-polarized light can yield information about the density of bulk electronic states of tungsten between the Fermi level and the vacuum level.

This paper is organized as follows. In Sec. II the theory of photofield emission is outlined, and in Sec. III the experimental procedures are described. The experimental data are presented and analyzed in Sec. IV. Finally, the conclusions of the work are summarized in Sec. V.

II. THEORY

Photofield emission may be described by considering a plane interface between a metal and the vacuum. When a strong negative static electric field is applied to the surface of the metal, the surface potential changes from a step to a roughly triangular barrier, through which conduction electrons may tunnel to the vacuum region. The tunneling current is termed "field emission." To observe field emission from tungsten, an electric field of the order of 0.2 V/Å is required. In order to obtain such a large field, the sample is chosen to be a thin wire, the end of which is electrochemically etched to form a cone with a hemispherical endcap (the "tip") of radius $\sim 0.1\ \mu$m. Because of its small size, the tip is a single crystal. It is not strictly hemispherical, but has facets typically 500×500 Å^2 developed normal to the low-index crystallographic directions. The sample is spot welded to a tungsten support loop, and mounted in an ultrahigh-vacuum chamber operating in the 10^{-11}-Torr range. A potential difference of ~ 2000 V applied between the tip and a conducting fluorescent screen creates the required field at the tip. The field-emission current causes fluorescence on the screen, and a characteristic light and a dark pattern is produced by variations in the work function from one tip facet to another. The form of the field-emission pattern indicates the state of cleanliness of the sample. The sample is cleaned whenever necessary by electrically heating the support loop to incandescence. Field emission from a single crystallographic plane may be selected by locating a small probe hole in the screen. The probe-hole current can be analyzed using appropriate electron optics to yield the total energy distribution of the electrons.

In photofield emission, laser light with a photon energy less than the work function of the metal is focused on the tip, and the total-energy distribution of the photoexcited electrons is measured. The coupled electron-photon system can be represented approximately by a simple single-particle model Hamiltonian of the form

$$H_0=-(\hbar^2/2m)\nabla^2+V(\mathbf{r})+H' , \tag{1}$$

where

$$V(\mathbf{r})=\begin{cases} V_c(\mathbf{r}), & z<0 , \\ V_s(z), & z>0 . \end{cases}$$

The crystal potential $V_c(\mathbf{r})$ is the periodic potential inside the metal. The potential $V_s(z)$ outside the metal has terms resulting from the applied electric field F and the image charge, and varies only in the direction of the surface normal $\hat{\mathbf{z}}$,

$$V_s(z)=-eFz-e^2/4z . \tag{2}$$

The perturbing electromagnetic dipole interaction which causes photoexcitation to occur is given by

$$H'=-[i\hbar e/(2mc)][\nabla\cdot\mathbf{A}(\mathbf{r})+\mathbf{A}(\mathbf{r})\cdot\nabla]e^{-i\omega t} , \tag{3}$$

where $-i\hbar\nabla$ is the electron momentum, and the monochromatic electromagnetic vector potential $\mathbf{A}(\mathbf{r})\exp(-i\omega t)$ is written in the gauge where the scalar potential is identically zero.

Inside the metal the eigenstates $|M\rangle$ of the system (M represents a set of quantum numbers) are solutions of the Schrödinger equation for the bulk crystal potential $V_c(\mathbf{r})$. Since a semi-infinite solid has translational symmetry parallel to the surface, these states may be expanded in functions whose variation parallel to the surface is described by plane waves with transverse momenta $\mathbf{k}_M+\mathbf{g}'$, where $\mathbf{k}_M$ is the reduced transverse wave vector in the first Brillouin zone, and $\mathbf{g}'$ is a surface reciprocal-lattice vector. In the vacuum region, the eigenstates are the product of two-dimensional plane waves of transverse wave vector $\mathbf{p}$ parallel to the interface and complicated tunneling functions in the z direction. Far from the surface, the tunneling function of energy E_M, transverse

momentum $\mathbf{p}$, and unit amplitude at the surface is given to a good approximation by a plane wave whose amplitude is equal to the transmission coefficient $T(W_M^p)$. $T(W_M^p)$ is an exponential function[11] of the normal energy

$$W_M^p = E_M^p - (\hbar^2/2m)p^2 . \quad (4)$$

Following the field-emission calculation of Nicolaou and Modinos[12] and the photoemission calculation of Schaich and Ashcroft,[13] the photofield emission excited from the initially unperturbed state $|L\rangle$ may be written as[14]

$$j_L = (2\pi e/\hbar)\sum_M \delta(E_L + \hbar\omega - E_M)\,|D_{ML}|^2 \times \sum_p |C_{Mp}^+|^2\,|T(W_M^p)|^2 . \quad (5)$$

In this expression the optical-transition matrix element D_{ML} from the initial state $|L\rangle$ to the final state $|M\rangle$ is given by

$$D_{ML} = -[i\hbar e/(2mc)]\langle M \,|\, \nabla\cdot\mathbf{A}(\mathbf{r}) + \mathbf{A}(\mathbf{r})\cdot\nabla \,|\, L\rangle . \quad (6)$$

The delta function allows transitions to a given final state $|M\rangle$ only if the transition conserves energy. The C_{Mp}^+ are the expansion coefficients required at the interface ($z=0$) to match the crystal state of energy E_M and transverse momentum $\mathbf{k}_M$ to the vacuum tunneling eigenfunction of energy E_M and transverse momentum $\mathbf{p}$ that propagates in the $+z$ direction. Transmission through an atomically smooth surface conserves the transverse momentum only to within a surface reciprocal-lattice vector $\mathbf{g}''$. Hence the sum over $\mathbf{p}$ includes all those transverse momenta that satisfy the condition

$$\mathbf{p} = \mathbf{k}_M + \mathbf{g}' + \mathbf{g}'' \equiv \mathbf{k}_M + \mathbf{g} . \quad (7)$$

The total energy distribution of photofield emission from all crystal states is

$$J(E) = \sum_L f(E_L) j_L [1 - f(E_M)]\delta(E - E_M) , \quad (8)$$

where $f(E)$ is the Fermi-Dirac distribution function.

A comparison with Eq. (5) demonstrates that the tunneling process plays an important role in determining the total-energy distribution of the emission current. Since the tunneling probability $|T(W_M^p)|^2$ depends exponentially on the normal energy, the greater part of the emission current will come from states having a large normal energy. An estimate based on the Wentzel-Kramers-Brillouin (WKB) approximation shows that under typical experimental conditions the probability of emission of an electron with a transverse wave vector of 0.15 Å^{-1} is 5% of that for an electron of zero transverse wave vector and the same energy. This is comparable to the transverse wave-vector resolution that can be achieved in inverse photoemission.[1] Recalling the definition of normal energy, it is clear that significant emission will occur only if $\mathbf{p}\simeq 0$. According to Eq. (7), this occurs when $\mathbf{k}_M + \mathbf{g} \simeq 0$. When $\mathbf{g}\simeq 0$, this condition represents emission from states close to the surface normal in the first Brillouin zone of the bulk metal. In the present paper, such emission processes will be termed *normal*. When $\mathbf{g}\neq 0$, this condition represents emission from states lying close to the surface normal in a higher zone in the extended zone scheme.[15] In the present paper, such emission processes will be termed *umklapp*. Umklapp processes may allow emission from final states that are not accessible in normal processes. Figure 1 illustrates this result for final states lying on a cross section through the zone center Γ normal to the $\langle 1\bar{1}0\rangle$ direction of the extended bulk Brillouin zone for a body-centered-cubic crystal. Consider for example emission from the (111) crystal plane. Figure 1 shows that states along ΓP are accessible in normal emission, while states along PH are accessible in umklapp emission. It will be seen that for emission from low-index planes such as (001) and (110), the final states accessible in the higher-order zones are equivalent to those in the first zone. For higher-index planes such as (111) and (211), additional final states on the face of the bulk Brillouin zone are accessible in higher-order zones.

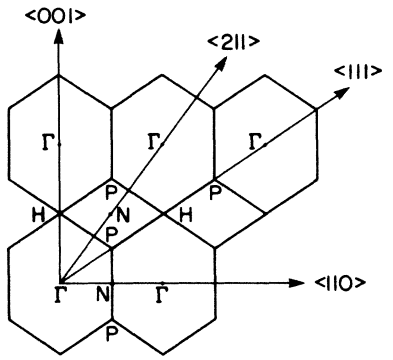

FIG. 1. A section through reciprocal space normal to the $\langle 110\rangle$ direction and including the zone center for a body-centered cubic lattice. Electrons from states lying on a given crystallographic axis but outside the first Brillouin zone of the bulk solid may be emitted from the plane normal to that axis by umklapp processes.

Another important consequence of the form of Eq. (5) is that photofield emission may be sensitive to surface electronic properties even if the optical excitation occurs in the bulk. This is because the contribution of each final state $|M\rangle$ to the external current is weighted by $|C_{Mp}^+|^2$. This weighting factor is closely related to the surface density of states, ρ_s, at the final-state energy

$$\rho_s(E) = \sum_M \delta(E - E_M)\sum_p (|C_{Mp}^+|^2 + |C_{Mp}^-|^2) . \quad (9)$$

In field emission, this sensitivity to the surface density of states (strongly weighted toward states with $k_M + g \simeq 0$) is the source of the structure in the total-energy distribution. In photofield emission, the optical-transition matrix elements are also expected to introduce structure into the total-energy distribution, but it is not clear *a priori* which effect will be dominant.

The matrix element D_{ML} describes the photoexcitation step in photofield emission. It is instructive to rewrite the matrix element in the form

$$D_{ML} = \beta\langle M \,|\, [\nabla\cdot\mathbf{A}(\mathbf{r})] \,|\, L\rangle + 2\beta\langle M \,|\, \mathbf{A}(\mathbf{r})\cdot\nabla \,|\, L\rangle , \quad (10)$$

where $\beta = -i\hbar e/2mc$. The first term in this equation

represents transitions induced by the spatial variation of the vector potential. For p-polarized light crossing a plane interface between the vacuum and a metal, the normal component of the vector potential will vary rapidly in the interface region and hence contribute to this term.[16] Since the present experiments are carried out with photons whose energy is well below the bulk plasmon energy, a large peak is expected to occur in the normal component of the vector potential just outside the surface of the metal.[17] Therefore, photofield emission in p-polarized light is expected to be very sensitive to surface excitation. Experiment has shown that the presence of even a small p-polarized component in the incident light beam would be sufficient to account for the failure of previous experimental studies of photofield-emission total-energy distributions[2,3] to detect departures from free-electron behavior due to bulk band-structure effects.

In order to discriminate against the photoexcitation occurring at the surface, the light must be incident with its polarization vector in the plane of the interface (i.e., s polarized). In this case the vector potential is continuous and does not vary rapidly in the surface region.[16,17] To a good approximation, the incident transverse electromagnetic wave is refracted and decays exponentially into the metal in agreement with the Fresnel equations.[18] Since the decay length of the wave is at least as large as the escape depth of the excited electrons in photofield emission, the spatial variation of $\mathbf{A}(\mathbf{r})$ is negligible for s-polarized light, and only the second term in the matrix element in Eq. (10) makes a significant contribution. Using a standard commutator identity,[13] that term may be rewritten as

$$D_{ML}=[2\beta/(\hbar\omega)]\mathbf{A}\cdot\langle M\,|\,\nabla V(\mathbf{r})\,|\,L\rangle\ , \tag{11}$$

where $V(\mathbf{r})$ is the electron potential given in Eq. (1). At the surface, the variation of the potential parallel to the surface is small in comparison with the variation in the direction of the surface normal. Since the light is s polarized, $\mathbf{A}\cdot\nabla V_s(\mathbf{r})$ is expected to be very small. Therefore, the principal contribution to the matrix element in Eq. (11) will come from photoexcitation in the bulk. While this matrix element describes only direct interband bulk excitations,[19] nondirect transitions mediated by phonons or other perturbations[20] may also occur.

If direct bulk transitions occur, then the distribution will depart from free-electron behavior at the energies of final states to which direct transitions are allowed. These features are expected to vary as the photon energy is varied. If nondirect transitions are important, and if all nondirect transitions are equally probable, then the distribution is expected to depart from free-electron behavior at those energies where there is a rapid variation in the product of the initial and final densities of states. In either case, the angular discrimination of the surface potential barrier will restrict the final states that contribute to the external current to those close to the emission direction in the extended zone in reciprocal space.

In order to identify departures from free-electron behavior due to bulk photoexcitation, it is useful to reduce Eq. (5) to the limit of the free-electron model. The potential in a free-electron metal is not periodic, so the sum over $\mathbf{p}$ collapses to the single term $\mathbf{p}=\mathbf{k}_M$. Since the crystal states are free-electron states, C^{+}_{Mp} is unity and the sums over L and M represent integrals over total momentum states $\mathbf{K}_L$ and $\mathbf{K}_M$. These integrals may be transformed to integrals over total energy, normal energy, and azimuthal angle, to yield

$$J(E)=[m^3e\Omega^2/(8\pi^5\hbar^7)]f(E-\hbar\omega)[1-f(E)]\times\int_{V_0}^{E-\hbar\omega}dW_L\,d\phi_L(W_L-V_0)^{-1/2}\times\int_{V_0}^{E}dW_M\,d\phi_M(W_M-V_0)^{-1/2}\,|\,D_{ML}\,|^2\,|\,T(W_M)\,|^2\ , \tag{12}$$

where Ω is a normalizing volume, and V_0 is the potential at the bottom of the free-electron conduction band. Bulk transitions in a free-electron metal must be nondirect. The matrix element for nondirect transitions is assumed to be a constant, $|\,D\,|^2$, for all initial and final states separated by the photon energy $\hbar\omega$. The barrier tunneling probability may be evaluated in the WKB approximation and expanded about $E_F+\hbar\omega$ as[11]

$$|\,T(W_M)\,|^2=e^{-c}e^{(W_M-E_F-\hbar\omega)/d}\ , \tag{13}$$

where c and d are defined in Ref. 11. Since the factor $(W_M-V_0)^{-1/2}$ varies slowly compared to the exponential, it may be approximated by its end point.

$$J(E)=[m^2\Omega^2/(\pi\hbar^4)][1-f(E)]\times|\,D\,|^2[(E-\hbar\omega-V_0)/(E-V_0)]^{1/2}J^{*}_{\mathrm{FE}}(E)\ , \tag{14a}$$

where

$$J^{*}_{\mathrm{FE}}(E)=[med/(2\pi^2\hbar^3)]f(E-\hbar\omega)\,|\,T(E)\,|^2 \tag{14b}$$

reduces to the field-emission current density[21] evaluated with an effective Fermi level of $E_F+\hbar\omega$.

The total-energy distribution in photofield emission from a free-electron metal is therefore given to a good approximation by shifting the field-emission distribution by the photon energy.[22] A plot of the logarithm of the current against total energy is roughly triangular in shape. The constant positive slope at low energy is $1/d$, and depends only on the barrier transmission. The constant negative slope at high energy is $1/d-1/kT$, and results from the barrier transmission and the cutoff of the Fermi occupation factor. Extrapolations of these constant slope regions intersect at $E_F+\hbar\omega$. Departures from free-electron behavior show up as changes in slope on the linear portions of the semilogarithmic plot, which occur at those energies where there is a change in the number of constant energy surfaces contributing to the emission current.

III. EXPERIMENT

The photofield-emission spectrometer used to measure the total-energy distributions has been described else-

where.[23] A diagram of the spectrometer is shown in Fig. 2. Two main improvements over the apparatus used in previous studies have made the present experiments possible. The first improvement is a sample positioner which allows the laser light to fall on any crystallographic facet developed on the field emitter with an arbitrary angle of incidence. By working at normal incidence, surface excitation due to small angular misalignments and to depolarization effects is minimized. The second improvement is the use of a deflection energy analyzer composed of two 127° cylindrical analyzers in tandem. This analyzer has a resolution function with a full width at half maximum height of $(0.0390\pm0.0006)E_0$, where E_0 is the pass kinetic energy of the analyzer, and a peak signal-to-noise ratio of 2×10^4. The large signal-to-noise ratio allows measurements of the total-energy distribution over more than 4 orders of magnitude.

An alignment procedure was devised to ensure that the light was properly focused on the tip at normal incidence. Potentials were applied to the deflector plates (see Fig. 2) to shift the field-emission pattern so that the probe hole in the screen sampled the appropriate region. The deflector potentials were adjusted iteratively with the tip position to maximize the detected field-emission signal. A field-emission total-energy distribution was measured to confirm that the electron optics were properly aligned. The laser light was then focused on the tip, and the position of the focal spot was adjusted to maximize the photofield-emission signal. The irradiance at the tip was less than 10^3 MW m^{-2}, and was therefore in the proven regime of one-photon excitation.[24] The temperature rise of the tip was typically less than 100 °C, and at all times less than 200 °C. A Pockels cell external to the vacuum system was used to control the angle of linear polarization of the light. A plot of the total photocurrent as a function of the voltage applied to the Pockels cell was recorded using a computer-controlled high-voltage supply. The dependence of the surface excitation component of the photocurrent on the light polarization is such that, at an arbitrary angle of incidence, the plot shows a sinusoidal variation. The ratio χ, defined as the ratio of the maximum photocurrent to the minimum photocurrent in the plot, serves as a measure of the angle of incidence.[9,14] When $\chi=1$, the normal component of the vector potential is zero for every direction of light polarization, and therefore normal incidence has been obtained. The ratio χ was measured from the plot, and systematic variations were made in the tip orientation angles θ and ϕ in Fig. 2 to minimize χ. Once these angles were changed, the entire alignment procedure was repeated. Thus the condition of normal light incidence was approached iteratively.

The limiting factor in the accuracy of the angle of incidence ψ was the determination, by eye, of when the probe hole sampled the appropriate region of the field-emission pattern. Because of this, the angle of incidence can be determined only to within about $\pm1°$. For a small misalignment, the ratio χ falls to between 1.01 and 1.20 for most of the planes which have been studied, and a small residual sinusoidal variation of the current with the polarization angle remains. It is conceivable that this is due not to the misalignment of ψ, but to a weak contribution from direct bulk excitation. Such an effect would be very difficult to study systematically because of its small size. It might also arise from a slight depolarization of the light. All the distributions reported here were recorded at the minimum of any residual variation of the photocurrent with polarization angle.

Total-energy distributions were recorded for the (100), (110), (111), (211), and (510) facets of tungsten. The light source was a krypton ion laser which can be tuned to eight discrete wavelengths spanning the visible and near ultraviolet, corresponding to photon energies between

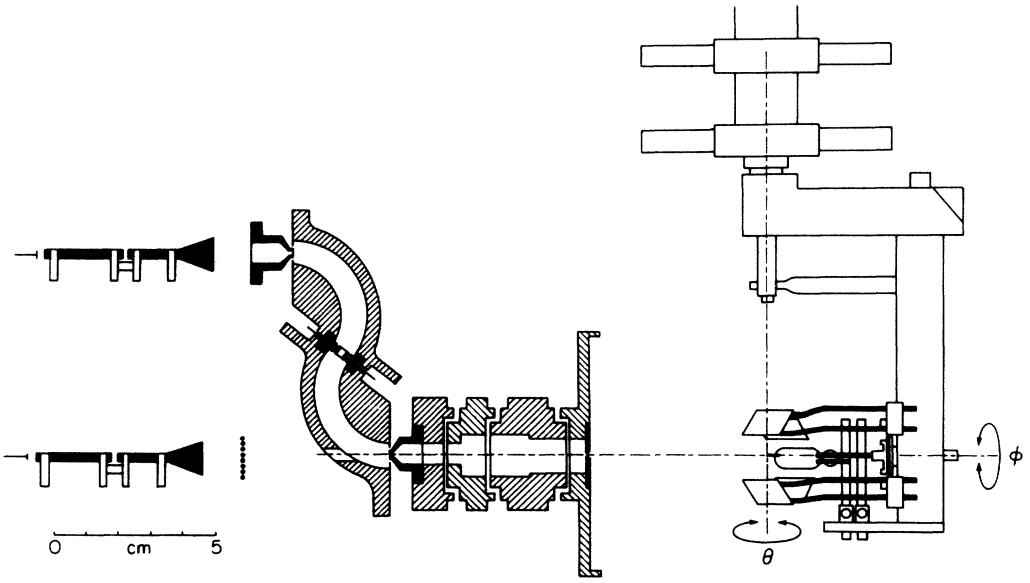

FIG. 2. The photofield-emission spectrometer. The tip may be rotated about two orthogonal axes and translated in three orthogonal directions. Deflector plates allow the emission pattern to be shifted on the screen. Electrons passing through the probe hole are decelerated and enter the deflection-energy analyzer.

1.916 and 3.536 eV. Low count rates on planes having large work functions, such as (110), made measurements at the lower photon energies very difficult. These data are not reported here since they have too much shot noise to be of use. Field-emission and photofield-emission distributions were recorded using a computer-controlled data acquisition system. The pass energy of the electron energy analyzer was set to 2 eV, giving a resolution function with a full width at half maximum height of approximately 80 meV ($\simeq$6 mRy). Each distribution was divided into about 100 equal intervals, or channels, each having a width of approximately 24 meV. The entire distribution was collected every 200 ms by sweeping through the channels sequentially and accumulating the counts in each channel for 2 ms. The results from each sweep were added to average out the effects of alignment drift and slow tip contamination. Data were accumulated for between 15 and 30 min, depending on the noise level. A Fowler-Nordheim plot was taken to establish the field constant of the facet. Typically, the field at which the distributions were measured was found to be within 10% of 0.25 V/Å.

If electron emission occurs by tunneling through the surface barrier, the gross features of the field-emission and photofield-emission total-energy distributions are determined by the exponential energy dependence of the surface-barrier transmission and of the Fermi occupation factor for initial-state electrons. These effects are well described by free-electron theory. However, the fine details of the total-energy distribution from a real metal are influenced by the densities of states and by optical transitions. In order to resolve the details of these features, it is necessary to remove the influence of the barrier transmission probability by subtracting the free-electron "background."

According to Eq. (14), the free-electron contribution to the photofield-emission distribution may be expressed as

$$\ln J(E)=\begin{cases}\ln A-(E-E_F-\hbar\omega)m_1, & E-E_F-\hbar\omega<-5kT\ , \quad (15a)\\ \ln A-(E-E_F-\hbar\omega)m_2, & E-E_F-\hbar\omega>5kT\ , \quad (15b)\end{cases}$$

where A is the amplitude of the distribution and the slopes m_1 and m_2 may be related to the temperature and applied field using results presented in Ref. 11. If straight lines are fitted to the linear portion of the logarithm of the distribution at high and low energy, the slopes and intercepts of these lines determine the four parameters A, E_F, m_1, and m_2. Such a fit is illustrated in Fig. 3(a). Here the photocurrent from the (111) plane of tungsten, illuminated with normally incident light of photon energy 2.604 eV, is plotted on an energy scale relative to E_F as determined by the fitting procedure.

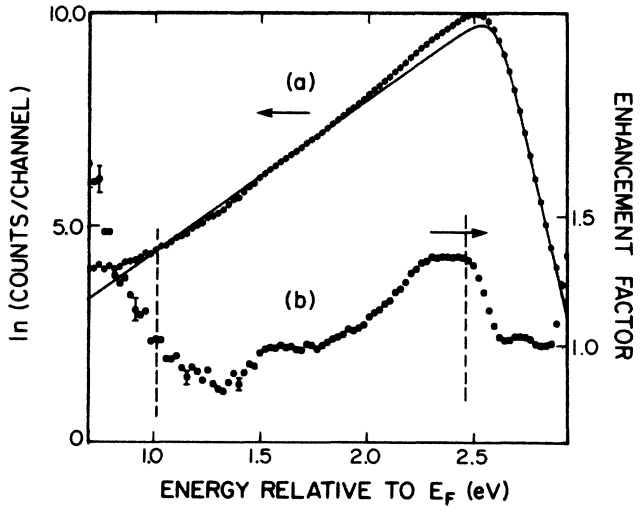

FIG. 3. Sample data analysis. Curve (a) shows the logarithm of the photofield-emission total-energy distribution from the (111) plane of tungsten with normally incident light of photon energy 2.604 eV. The solid curve is the fitted free-electron background. Curve (b) is the resulting enhancement factor. The dashed lines indicate the energies between which the enhancement factor is reproducible.

At energies between 1.2 and 1.5 eV and between 1.8 and 2.6 eV, the data show reproducible departures from free-electron theory. To bring these features into greater prominence, an enhancement factor $R(E)$ was defined as the difference between the natural logarithms of the experimental and fitted free-electron curves,

$$R(E)\equiv\ln J_{\text{expt}}(E)-\ln J_{\text{fit}}(E)\ . \quad (16)$$

The enhancement factor calculated from the data in Fig. 3(a) is shown in Fig. 3(b). Errors due to counting statistics are greatly magnified by the subtraction of the exponential free-electron background and are indicated by the error bars in various regions of the curve. Between 2.0 and 2.4 eV the error bars are no larger than the plotted symbols. The error bars are seen to correspond roughly to the scatter in the data points.

The energy range containing useful information is restricted to the linear portion of the low-energy side of the fitted distribution. The linear portion of the high-energy side of the distribution is so steep that deviations from linearity cannot be reliably detected. The rounded portion at the apex of the fitted distribution is the energy range where the Fermi function varies most rapidly. Structure in this region of the enhancement factor is sensitive to small changes in the fit, and is not reproducible. The large enhancement factor at energies below 1.2 eV is caused by the field emission overlapping with the photofield emission. Therefore, only the portion of the curve between the dashed lines in curve 3(b) is considered in the analysis of the distributions.

Analysis of data by the two-slope method based on Eq. (15) is valid only if electron emission occurs by tunneling through the surface potential barrier. At a sufficiently high photon energy electrons are emitted above the peak

of the surface barrier, and the transmission probability no longer depends exponentially on the normal energy [cf. Eq. (13)]. This results in a broadening and a flattening of the peak of the total-energy distribution, and analysis by the two-slope method fails to yield a value of the Fermi energy that is consistent from crystal plane to crystal plane. In the present experiments, only data taken at the highest photon energy (3.536 eV) show evidence of emission above the peak of the surface barrier.

In photofield emission, high resolution for states with small transverse wave vectors is achieved only if emission occurs by tunneling through the surface barrier. If electrons are emitted above the peak of the barrier, significant emission occurs from states having large transverse wave vectors. Even though structure may still be observed in the total-energy distribution, it is not expected to be related in any simple way to the electronic states along the emission direction in the bulk Brillouin zone. In the present paper, data showing evidence of emission above the peak of the surface barrier are included for completeness. However, the interpretation of the features observed in these data (Table II) must be considered less reliable than that of features observed in the tunneling data (Table I).

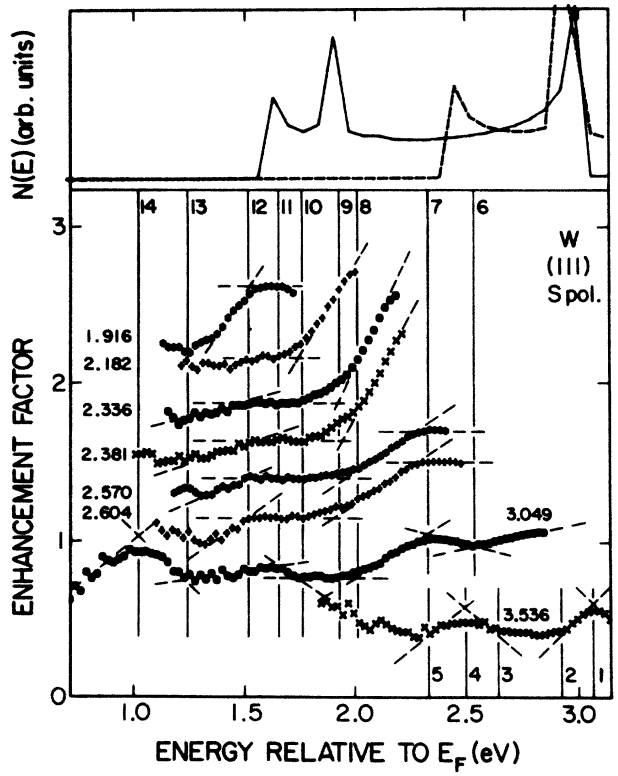

FIG. 4. Enhancement factors (expressed as the natural logarithm) for photofield emission from the (111) plane of tungsten with normally incident light. Each curve is labeled by the appropriate photon energy. The curves have been displaced vertically for clarity. Vertical lines mark the mean energy of qualitatively similar features. The numbering of the lines refers to Table I. $N(E)$ is the one-dimensional density of states accessible in normal transitions (solid line) and umklapp transitions (dashed line) calculated from the potential V_2 of Ref. 27.

IV. RESULTS

Enhancement factors observed at the various photon energies for the (111), (211), (100), (510), and (110) facets of tungsten are presented in Figs. 4, 5, 6, 7, and 8, respectively. The data are plotted against energy relative to the Fermi energy. The Fermi energy was estimated by averaging the fitted Fermi energies for all the data from all facets, and has an uncertainty of ± 7 meV. The data set for the (110) plane was collected with s-polarized light at an angle of incidence of 20° instead of at normal incidence, since the sample positioner blocks the scattered light at smaller angles of incidence on this plane, making it difficult to position the focal spot. Each curve is labeled with the appropriate photon energy. A change in slope in the enhancement factor is considered to be a "feature" which departs from free-electron theory. The energy at which the feature occurs is found by extrapolating linear portions of the enhancement factor, as is indicated in the plots by the dashed lines.

Experimental studies of the polarization dependence of photofield emission have shown that the total emission current in p polarization is always greater than that in s polarization, their ratio being a function of the angle of incidence.[4] A comparison of the enhancement factors from any single crystal plane with those obtained from the same plane in a separate study[23,25] using p-polarized light at grazing incidence (so that surface excitation is ex-

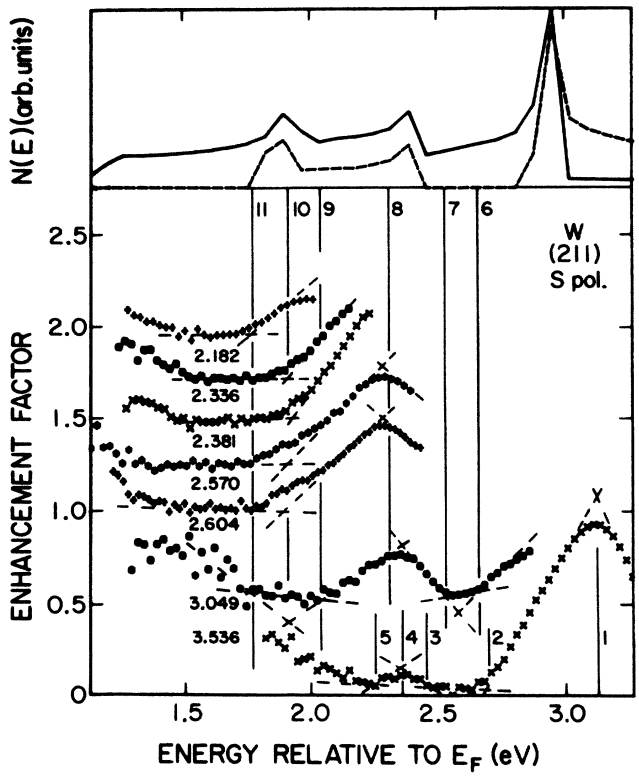

FIG. 5. Enhancement factors (expressed as the natural logarithm) for photofield emission from the (211) plane of tungsten with normally incident light. The plotting conventions are defined in the caption to Fig. 4.

pected to dominate) shows that the enhancement factors for s- and p-polarized light are very different. This is strong evidence to support the conclusion of Venus and Lee[4,9] that different photoexcitation mechanisms predominate in the two configurations. Since the s- and p-polarized data sets have few features in common, it appears that the contributions of the two excitation mechanisms can be effectively separated by selecting the polarization angle and angle of light incidence.

The enhancement factors in each data set have many features that occur at a constant energy relative to E_F. An analysis of the consistency of these features is presented in Table I. For the reasons discussed above, Table I includes only features observed at a photon energy of 3.049 eV or less, corresponding to emission by tunneling through the surface barrier. Vertical lines are drawn on the plots at the mean energy relative to E_F for the occurrence of qualitatively similar features within a data set. Each line is labeled with a number which refers to the appropriate entry in Table I for that plane. The uncertainty in the energy (σ), and the number of different photon energies at which the feature is observed, are also recorded. If a feature is observed at only two photon energies, the uncertainty is taken as the range of the values. If a feature is observed at only one photon energy, no uncertainty is quoted. Some features are grouped together in the table and are termed a "structure" for ease of discussion. On many of the planes, the uncertainties in energy

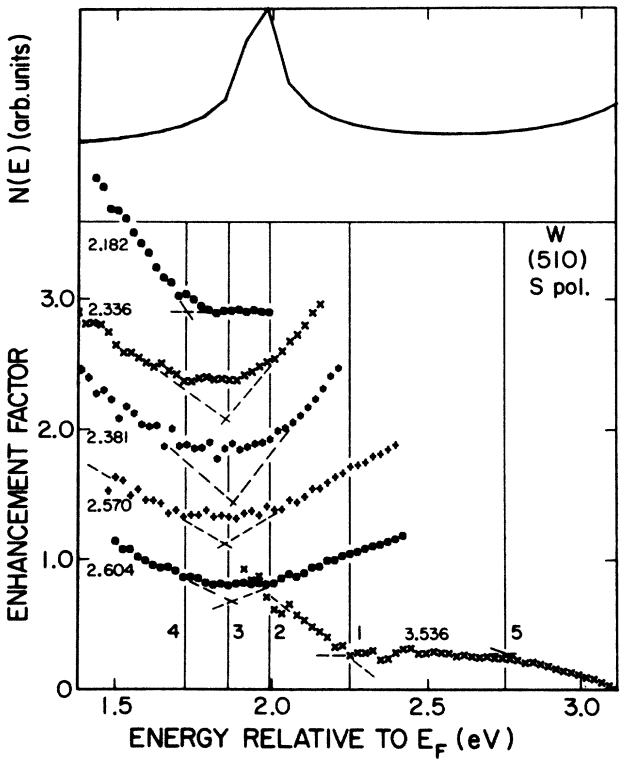

FIG. 7. Enhancement factors (expressed as the natural logarithm) for photofield emission from the (510) plane of tungsten with normally incident light. The plotting conventions are defined in the caption to Fig. 4.

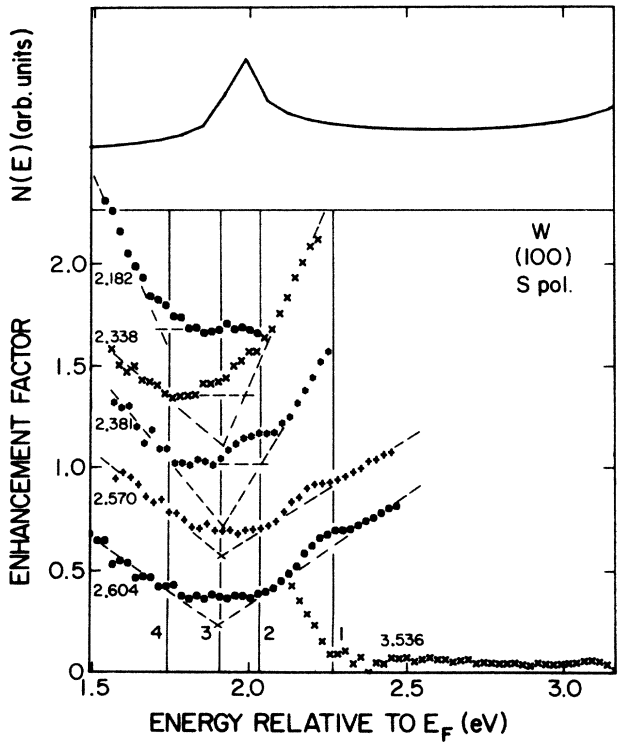

FIG. 6. Enhancement factors (expressed as the natural logarithm) for photofield emission from the (100) plane of tungsten with normally incident light. The plotting conventions are defined in the caption to Fig. 4.

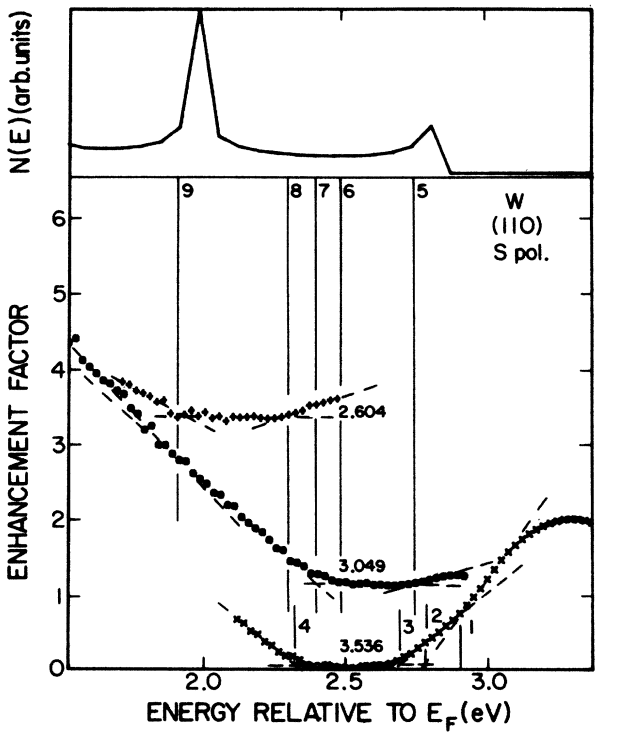

FIG. 8. Enhancement factors (expressed as the natural logarithm) for photofield emission from the (110) plane of tungsten with s-polarized light incident at 20°. The plotting conventions are defined in the caption to Fig. 4.

are comparable to the uncertainty in determining the Fermi energy and are of the order of the channel width (24 mV). Thus most of the features are seen to occur at a constant energy independent of the photon energy.

At least one feature does not occur at a constant energy. There is a prominent feature in the data set measured on the (100) plane which occurs at a decreasing energy as the photon energy is decreased. The (100) plane of tungsten has a prominent surface resonance approximately 0.36 eV below the Fermi energy. This surface resonance was originally observed in field emission,[26] and has been studied with photoemission[27] and photofield-emission techniques.[5,25] To test whether residual coupling to the surface resonance is responsible for the observed feature, the data in Fig. 6 are replotted in Fig. 9 against energy relative to $E_F+\hbar\omega$, and the expected energy of the peak due to excitation from the resonance is marked by a vertical line. The good agreement between the peak position and the vertical line indicates that the peak is almost certainly an initial-state effect due to the surface resonance on the (100) plane. Choosing normally incident light is expected to extinguish surface photoexcitation from this state. In fact, the emission is reduced by a factor of 350 compared to that observed in p-polarized light at grazing incidence.[25] The small residual coupling to the surface state might result from surface photoexcitation caused by a small angular misalignment or a slight depolarization of the light. It might also be due to a more subtle effect. Weng, Plummer, and Gustafsson[27] have found evidence that this surface resonance contains some small mixture of wave functions of odd symmetry and is therefore weakly excited by s-polarized light. The precise nature of the photoexcitation mechanism is not clear.

Comparison to the bulk band-structure calculation of Christensen and Feuerbacher,[28] which is known to give generally good agreement with experimental Fermi surface and photoemission data,[29] shows that many features in the experimental enhancement factors occur at energies where direct bulk are not possible. A few of the features in some enhancement factors are consistent with direct bulk transitions, but the features do not disperse with photon energy, whereas the band-structure calculation suggests that they should. If the photocurrent is due to nondirect bulk transitions, the features in the enhancement factors that occur at the same energy independent of photon energy should correspond to rapid variations in

TABLE I. Summary of features in the data sets for emission through the barrier ($\hbar\omega \leq 3.049$ eV). The No. heading denotes the number of different photon energies at which a feature is observed.

Plane	Structure	Feature	No.	$(E-E_F)\pm\sigma$ (eV)	Bulk band region	Calculated energy (eV)
(111)	B	6	1	2.530		
		7	3	2.295±0.024	F_6 band minimum	2.422
	D	8	5	2.006±0.021		
		9	5	1.912±0.031	Γ_8^+	1.986
		10	6	1.758±0.018		
	C	11	1	1.655	?	
	E	12	6	1.523±0.008	Λ_4 band minimum	1.604
	F	13	1	1.248	Initial DOS	
		14	1	1.057	($\hbar\omega=3.049$ eV)	
(211)	J	6	1	2.657	Band minimum at BZ	2.803
	K	7	1	2.535		
		8	3	2.326±0.045	Band maximum at BZ	2.463
	M	9	5	2.061±0.040		
		10	5	1.941±0.018	Γ_8^+	1.986
		11	6	1.803±0.047		
(100)	R	2	4	2.016±0.029		
		3	4	1.925±0.008	Γ_8^+	1.986
		4	5	1.781±0.037		
(510)	T	2	4	1.991±0.019		
		3	4	1.863±0.011	Γ_8^+	1.986
		4	5	1.724±0.038		
(110)	V	5	1	2.702	Onset of N_5^+	
	W	6	1	2.482		
		7	1	2.398	?	
		8	1	2.294		
	X	9	2	1.915±0.012	Γ_8^+	1.986

the product of the initial and final densities of states. For photon energies less than 3.049 eV, the measurements sample the initial density-of-states curve only from -1.1 eV to the Fermi level. The density of states calculated from the potential V_2 of Christensen and Feuerbacher,[28] is plotted at the top of Fig. 10. One can see that the total bulk density of states of tungsten has very little structure in this energy range.[28] Rapid changes in the product of the initial and final densities of states will therefore reflect, to a good approximation, variations in the final density of states alone. So long as emission occurs by tunneling through the surface barrier, only those final states that are close to the emission axis in the extended zone scheme will give an appreciable contribution to the external current. For measurements made using photon energies of 3.049 and 3.536 eV, the structure in the total initial density of states at energies below -1.1 eV may be observable as features in the enhancement factor at low energy.

To test whether the features of the observed distributions are correlated with high density-of-states regions, the one-dimensional bulk densities of states for tungsten for the appropriate crystallographic directions have been calculated from the potential V_2. The results are plotted at the top of Figs. 4—8. The solid curves are the densities of states within the first bulk Brillouin zone and the dashed curves are the densities of additional bulk states from which electrons may be emitted by umklapp processes. A comparison of the energies of features observed in the enhancement factors, and of peaks in the corresponding one-dimensional density of final states, is summarized in Tables I and II. Many of the features coincide with high density-of-states regions near the Brillouin-zone centre, at the Brillouin-zone boundary, or at energy-band extrema at intermediate wave vectors. A description of these high density-of-states regions, and their calculated energies, are given in the final two columns of the tables. They are also marked on the bulk band structure in Fig. 11. The features attributed to a large initial density of states will be discussed below.

The photofield-emission enhancement factors observed in the tunneling regime (i.e., $\hbar\omega \lesssim 3.049$ eV) are summarized in Table I. The enhancement factors from the (111) plane are plotted in Fig. 4. They have a total of four main structures, or groups of features. Feature 7 is attributed to the F_6 band minimum, which is accessible by umklapp transitions. The next three features, 8, 9, and 10, are grouped together as structure D. The middle

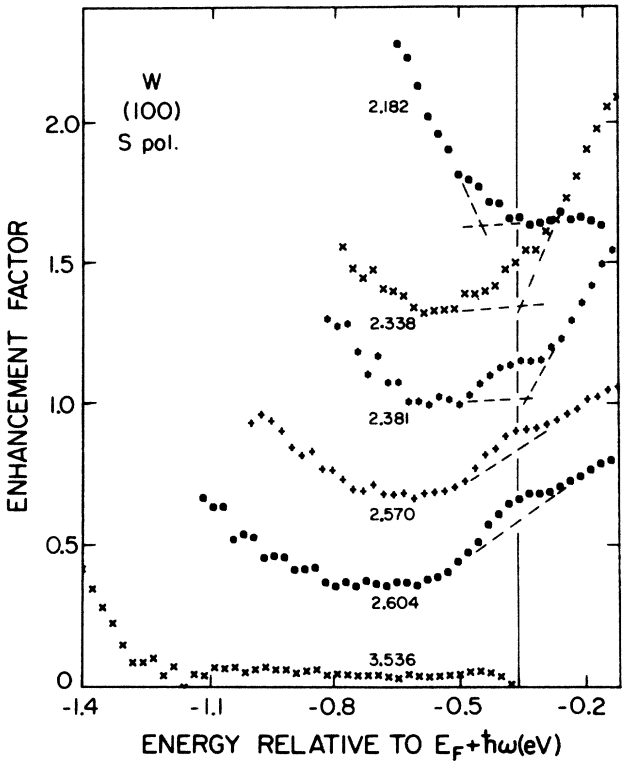

FIG. 9. The data set for light at normal incidence on the (100) plane (Fig. 6) is replotted against energy relative to $E+\hbar\omega$. The curves have been displaced vertically for clarity. The vertical line marks the energy at which the surface resonance on the (100) plane occurs.

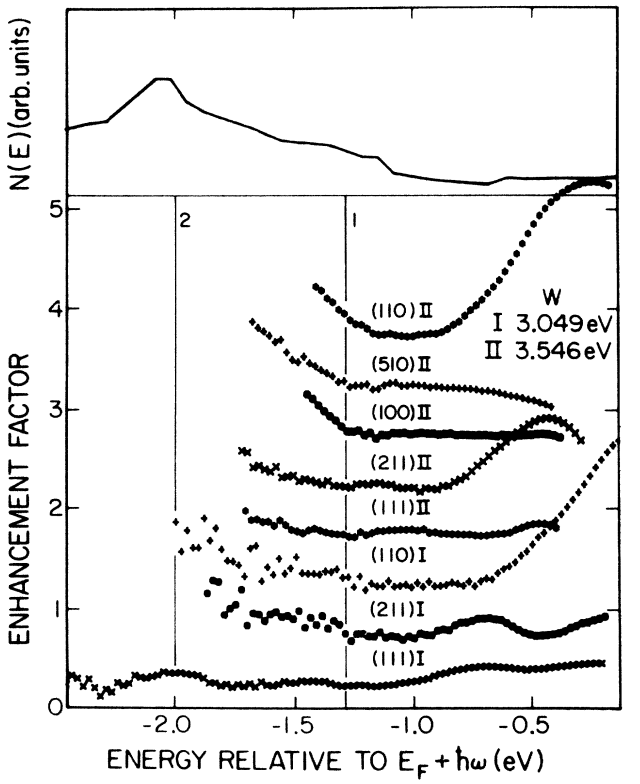

FIG. 10. Enhancement factors (expressed as the natural logarithm) for photofield emission with normally-incident light of photon energy 3.049 eV (denoted I) and 3.535 eV (denoted II). Each curve is labeled by the appropriate plane indices. The curves have been displaced vertically for clarity. The vertical line (1) marks the mean energy below which the enhancement factors, on all crystal planes and at both photon energies, increase rapidly. $N(E)$ is the total density of initial states as calculated from the potential V_2 of Christensen and Feuerbacher (Ref. 28).

TABLE II. Summary of features in the data sets of emission above the barrier ($\hbar\omega = 3.536$ eV). The No. heading denotes the number of different photon energies at which a feature is observed.

Plane	Structure	Feature	No.	$(E-E_F)+\sigma$ (eV)	Bulk band region	Calculated energy (eV)
(111)	*A*	1	1	3.07	*P*	3.102
		2	1	2.91	F_4^8 band minimum	2.898
	B	3	1	2.64		
		4	1	2.47	F_6 band minimum	2.442
		5	1	2.30	Initial DOS?	
(211)	*J*	1	1	3.12	Band minimum maximum	2.939,3.279
		2	1	2.70	Band minimum	2.803
	K	3	1	2.47	Band maximum near	
		4	1	2.39	BZ	2.463
		5	1	2.25	Initial DOS?	
(100)	*Q*	1	1	2.26	Initial DOS	
(510)	*S*	1	1	2.25	Initial DOS	
	U	5	1	2.75	Barrier peak?	
(110)	*V*	1	1	2.91		
		2	1	2.79	N_5^+	2.891
		3	1	2.71		
	W	4	1	2.32	?	

feature is the intersection of the extrapolation of linear portions of the enhancement factor on either side of a change of slope. It is attributed to the high density-of-states region of symmetry Γ_8^+ at the zone center. Features 8 and 10 mark the energies at which the data curve departs from the linear extrapolations, and give an estimate of the energy width of the high density-of-states region. The identification of this feature with a high density-of-states region near the zone center is strongly supported by the fact that similar structures are observed in the enhancement factors measured on all five planes in the present study. Only the region near Γ is close to the normal direction for all of these planes. Feature 11, which occurs only in the data set with $\hbar\omega = 3.049$ eV, is not identified. Feature 12 is attributed to the minimum of a Λ_4 energy band. This feature occurs in the enhancement factors for six different photon energies, but the magnitude of the effect is dependent on the photon energy.

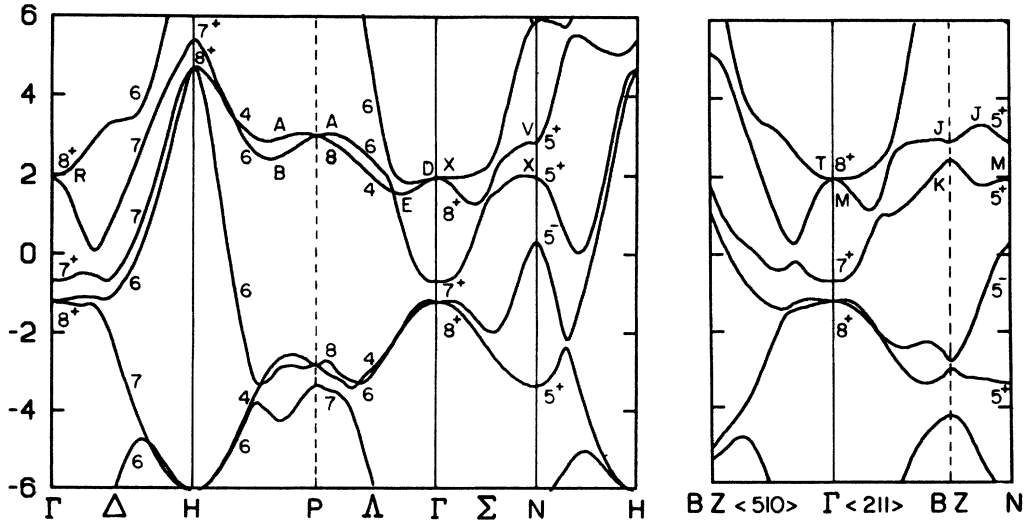

FIG. 11. The band structure of tungsten near the Fermi level, calculated from the potential V_2 of Christensen and Feuerbacher (Ref. 28). The appropriate group names label the symmetry points and the bands. The capital letters label high density-of-states regions that are assigned to the corresponding structures in Tables I and II. Energy scale in eV relative to E_F.

Features 13 and 14 occur only at a photon energy of 3.049 eV. They are interpreted as initial-state effects and are discussed below. At lower energies the enhancement factors increase again due to the high-energy tail of the field-emission distribution.

The enhancement factors in the data set measured from the (211) plane and plotted in Fig. 5 are very similar to those measured from the (111) plane. These two directions are separated by only 20°, and the bulk bands are similar along the two axes. Two bands, which are degenerate at P along the $\langle 111 \rangle$ direction, split for wave vectors away from P and are separated by about 0.4 eV for the Brillouin-zone boundary along the $\langle 211 \rangle$ direction. The upper band has a minimum at the zone boundary, which is observed as feature 6. The lower band has a maximum near the Brillouin-zone boundary, and the peak and baseline energies of this high density-of-states region are marked by structure K. The three features that constitute structure M are attributed to the high density-of-states region of symmetry Γ_8^+. Feature 12 in the data set from the (111) plane is absent from the present data set. This is to be expected, because the band minimum along the $\langle 111 \rangle$ axis disperses to lower energy away from the $\langle 111 \rangle$ axis. Along the $\langle 211 \rangle$ axis this minimum is at too low an energy to be observed in the data. The increase in the enhancement factors at low energy is again due to the high-energy tail of the field-emission distribution.

The $\langle 100 \rangle$ and $\langle 510 \rangle$ directions are separated by only 11°, and therefore have enhancement factors (see Figs. 6 and 7) that are very similar. Features 2—4 are attributed to the Γ_8^+ symmetry point in both data sets.

The high work function of the (110) plane makes data collection from this plane very slow even at the highest photon energies. Accordingly, the data set measured from the (110) plane and plotted in Fig. 8 contains enhancement factors for only the three highest photon energies. Feature 5 is attributed to the onset of a structure due to a high density-of-states region at a N_5^+ symmetry point at an energy slightly too high to be seen with this photon energy. Features 6, 7, and 8 have no obvious explanation in terms of the one-dimensional density of states along the $\langle 110 \rangle$ axis. It is possible that this is a surface-sensitive structure that cannot be explained in terms of the bulk band structure. If it is the result of a large wave-function probability density $|C_{Mp}^+|^2$ at the surface, then only a full calculation of the surface band structure will suffice. Feature 9 occurs at an energy that is consistent with high density-of-states regions of symmetry Γ_8^+ and N_5^+. In all of the other data sets this Γ_8^+ point is marked by three features corresponding to a peak energy and an upper and lower bound in the high density-of-states region. Further experiments at other photon energies are required to substantiate the interpretation of this feature on this plane.

Features observed only in total-energy distributions for emission above the peak of the surface barrier (with a photon energy of 3.546 eV) are reported in Table II. The interpretation of these features in terms of a one-dimensional density of states is questionable because when emission occurs above the peak of the surface barrier, significant emission occurs from states with larger transverse wave vectors. Hence both the energies and the interpretations must be considered less reliable than those reported in Table I.

Feature 1 in emission from (111) is attributed to the high density-of-states region of symmetry P_8 at the zone corner. This feature was first tentatively identified in photofield-emission distributions by Venus and Lee.[4] Feature 2 is attributed to a minimum in an F_4 energy band and is therefore due to electrons emitted from the (111) plane by an umklapp process. The three features in the next structure are attributed to the peak and two baseline energies of the high density-of-states region which is accessible by umklapp processes. This is the minimum of an F_6 energy band midway between H and P. This feature was also observed in the tunneling emission, and appears somewhat higher in energy in the present data.

Features 1 and 2 in emission from (211) are attributed to a high density-of-states region associated with the upper band along $\langle 211 \rangle$. This peak is very broad because the energy band has very little dispersion from approximately two thirds of the way between Γ and the Brillouin-zone edge all the way to the N symmetry point (which can be reached by umklapp processes—see Fig. 1). The band has zero slope both very close to the Brillouin-zone boundary and also approximately midway between the Brillouin-zone boundary and N. The closely spaced energies at which these two high density-of-states regions occur are recorded in Table II opposite feature 1. The maximum of the experimental peak lies between them. Features 3, 4, and 5 correspond to the band maximum near the zone boundary that was also observed (at a slightly lower energy) in tunneling. A comparison of the data sets for (100) and (510) shows that (510) has an extra feature (labeled 5) close to the peak of the total-energy distribution. This weak feature cannot be explained in terms of the one-dimensional density of states. It has negative curvature in the raw data and is therefore possibly due to the broadening of the peak of the total-energy distribution that is associated with emission above the peak of the surface barrier. The data set from the (110) plane shows two structures. Structure V is attributed to an N_5^+ symmetry point at the Brillouin-zone boundary. Only the onset of this structure is seen in the tunneling data. Feature 4 is thought to correspond to structure W in the tunneling data, and has no explanation in terms of the one-dimensional bulk band structure.

The remaining features in Tables I and II are attributed to initial density-of-states effects. In Fig. 10, the data at 3.049 and 3.546 eV are replotted as a function of the initial-state energy. The vertical line (1) marks the energy below which the enhancement factors, on all planes and at both photon energies, increase rapidly. The onset of the rapid rise (which is somewhat muted by the compressed vertical scale of Fig. 10) is found to occur at an initial-state energy of -1.27 ± 0.05 eV. The total bulk density of states for tungsten,[28] which is plotted along the top of Fig. 10, shows that below this energy the total initial density of states is no longer approximately constant, but increases rapidly with decreasing energy. This is due to a high density-of-states region near the symmetry point Γ_8^+ at an energy calculated to be -1.17 eV. The field-emission enhancement factors[7] suggest that this region occurs at

between -1.2 and -1.4 eV. This feature is therefore attributed to a high density of initial states. It is not observed for other photon energies since these data do not sample initial states so low in energy. The strong peak (features 13 and 14) in the data set from (111) is attributed to a peak in the initial density of states which occurs approximately 2.0 eV below the Fermi level.

The good agreement between the experimental features and the product of initial and final densities of states supports the hypothesis that nondirect bulk transitions are responsible for the photocurrent. However, it is not clear why nondirect transitions should be so important in photofield emission. The absence of clear evidence for direct transitions is consistent with earlier polarization studies of photofield emission,[9] but in contrast to what might be expected by extrapolating the results of the related technique of photoemission to lower-photon energy. In angle-resolved photoemission, the energy distributions are often dominated by peaks due to direct interband transitions which disperse as the photon energy is changed.[29,30] Those cases where the spectra reflect the density of states are usually special circumstances where a role is played by coupling to holes in core states[31] or in ionically bound crystals,[32] or where crystal disorder due to phonons becomes significant in materials with very low Debye temperatures.[33] None of these effects is expected to be significant in tungsten in the energy range probed by photofield emission.

One possible explanation for the difference between the photoemission and photofield-emission results is that the matrix elements for direct interband transitions in the energy range probed by photofield emission may be small. That interband transitions between predominantly *d*-like states in tungsten are weak may be a consequence of the electric dipole selection rules,[34,35] according to which the initial and final states in such a transition must satisfy $\Delta L = \pm 1$. At low-photon energies, both the initial and the final states in tungsten are predominantly *d*-like. In these circumstances, a secondary process such as nondirect transitions could dominate the bulk photocurrent and the spectra would show the observed dependence on the final density of state. This interpretation is supported by the recent identification of a direct transition in photofield emission from the (110) plane of tungsten. In this experiment a *p*-like state just above the Fermi level was populated thermally, and transitions to a *d*-like final state were observed.[36]

A second possible explanation for the different character of the spectral features observed in photofield emission rests on the fact that barrier transmission effects are much more important than in photoemission. As was discussed in Sec. II, photofield emission may be surface sensitive because the tunneling process weights the emission by the surface density of states at $\mathbf{k}=\mathbf{0}$. It may be that this factor is of overriding importance and that, given some photoexcitation in the bulk, the observed features are not directly related to the optical transitions but rather to the variation in the surface density of states. Since discontinuities of slope in the surface density of states at $\mathbf{k}=\mathbf{0}$ are expected to coincide with the band limits of the one-dimensional bulk energy bands in the direction of the surface normal,[37] the good agreement between the experimental features and the energies where a large bulk density of state occurs is consistent with this hypothesis.

In summary, the enhancement factors support the hypothesis that bulk photoexcitation is primarily responsible for photofield emission observed in *s*-polarized light. The curves are qualitatively different from those observed in *p*-polarized light at grazing incidence,[25] where the surface photoeffect makes the dominant contribution to photofield emission. Most of the features occur at energies that coincide with a high density of initial or final bulk states. Since the total density of initial states is nearly constant in the energy range just below the Fermi level, most of the features correspond to final-state effects and occur at a constant energy relative to the Fermi energy regardless of photon energy. In fact, there is no high density-of-states region in the final-state energy range spanned by these measurements that cannot reasonably be assigned to some feature in the enhancement factors. These results are those expected for nondirect bulk transitions involving a third body, such as a phonon, between initial and final electronic states separated by one-photon energy. It is not clear, however, why nondirect transitions should dominate the photofield-emission spectra.

Since the present experiments are the first to measure the photofield-emission distributions with sufficient accuracy to detect departures from free-electron behavior due to bulk band-structure effects, direct comparison with other work is not possible. The results of Venus and Lee[4,9] concerning the polarization dependence of the energy-integrated photocurrent are reproduced in detail by the present experiments. Radoń,[38] and Radoń and Kleint,[39] have measured the energy-integrated photocurrent as a function of the applied field, and have plotted the logarithm of the current against the reciprocal of the field. Their modified Fowler-Nordheim plots show various shoulders and bumps that are interpreted as resulting from an increase in photofield emission whenever electrons at a well-defined final-state energy have just sufficient normal energy to pass over the peak of the surface potential barrier. They identify various direct and indirect bulk interband transitions that could account for the observed features. They investigate emission over a large energy range by adsorbing a layer of barium onto the field emitter to reduce its work function.

Radoń reports results for the (111) and (310) planes of tungsten, but does not indicate the angle of incidence or the direction of polarization of the incident light. If the light was *s* polarized, then some of the final-state effects that he reports are consistent with the present results. Specifically, he finds transitions to the Γ_8^+ symmetry point in the data from both planes and to the minimum in the Λ_4 band in the $\langle 111 \rangle$ direction in the data from the (111) plane. He also finds direct transitions to a quickly dispersing band along the $\langle 111 \rangle$ direction at an energy lower than that probed by the present experiments. However, if the light was *s* polarized it would appear to be fortuitous. It is more likely that there was some component of the polarization vector normal to the emitting plane. If this was the case, then surface photoexcitation would be predominant[5,25] and it is difficult to imagine that bulk

transitions could be detected.

Other questions complicate the interpretation of Radoń's results. The photofield-emission current is separated from a field-emission background approximately 10^6 times as large by chopping the laser beam at 1000 Hz and using phase-sensitive detection. Heating of the tip by the laser beam will occur on a time scale[40,41] of 10^{-5}–10^{-4} s, resulting in a temperature-induced increase in the field-emission background which cannot be removed by the phase-sensitive detection technique. It is therefore not certain that all of the observed structure can be attributed to changes in the photofield emission. Heating of the tip may be responsible for some reported data curves which are insensitive to the applied field and which appear to represent photoyield efficiencies as large as 20%.

Momentum-resolved inverse photoemission spectroscopy[42] results for tungsten have not yet been reported. Some early experiments using an electron beam which was not well collimated have been reported for a polycrystalline sample of tungsten.[43,44] The energy resolution in these experiments was approximately 700 meV and a large background of scattered electrons complicated the data analysis. A peak in the inverse photoemission spectrum at approximately 3 eV above the Fermi level may represent the same high density-of-states region near P which is observed in photofield emission from the (111) plane. (See structure A in Table II.)

The present results suggest a range of further experimental and theoretical investigations. It is necessary to address the question of why the enhancement factors in photofield emission should show structure that coincides with peaks in the one-dimensional bulk density of states. Studies of materials other than tungsten are required to see if this is a general result. If nondirect transitions are responsible, the nature of the third body involved in the process is as yet unclear. It might be studied by measuring the temperature dependence of photofield emission in s-polarized light. If phonons are the third body, changes in the phonon population due to temperature should affect the intensity of the photocurrent for normally incident light. If, instead, the tunneling process itself is responsible, then photofield emission may provide a method for probing directly the electronic surface density of states in the energy range between the vacuum level and the Fermi level. Studies of emission from adsorbate covered tips may provide insight into this possibility.

More realistic theoretical calculations are also required. The present analysis relies on calculations of the bulk electronic structure to describe a process that is sensitive to surface properties. While this approach gives a satisfactory account of the energies at which departures from free-electron behavior are observed, it is evident that a full understanding of the enhancement factors must await a calculation of the electronic structure of the metal half-space, and of the details of the matching conditions for the wave functions when tunneling occurs. Such calculations have been performed for low-energy electron diffraction experiments,[45] for photoemission experiments,[46] and to a lesser extent for field-emission experiments.[12] The results of these calculations should serve to test the present conclusions, to make it possible to interpret the dependence of the amplitude of features in the enhancement factors on photon energy, and to account for those features that do not correspond to high density-of-states regions in the bulk.

V. CONCLUSIONS

Photofield-emission total-energy distributions measured on five crystallographic planes of a tungsten field emitter at eight photon energies ranging from 1.916 to 3.536 eV are reported. The use of a deflection-energy analyzer with a large signal-to-noise ratio and of light normally incident on the emitting facet of the field emitter have made it possible to observe departures from free-electron behavior which show up as peaks or as changes of slope in the enhancement factors calculated from the distributions. The energies at which the departures from free-electron behavior occur are found to agree closely with the energies where rapid changes occur in the one-dimensional bulk density of states along the direction of emission.

The measurement of photofield-emission energy distributions has been shown to yield information about the bulk electronic states of a crystal between the Fermi level and the vacuum level. Combining this information with the results of Fermi surface studies should provide a detailed account of the energy bands in this energy range. A comparison of the present results with the predictions of self-consistent energy band-structure calculations involving differing treatments of exchange and correlation will be reported elsewhere.

ACKNOWLEDGMENTS

We are grateful to P. Donders for many discussions and for his help in solving numerous problems, and to N. E. Christensen for sending us details of the potential. The technical assistance of K. Weisser of the Scarborough Academic Workshop and J. Shuve of the Electronics Workshop are much appreciated. This work was supported in part by operating and equipment grants from the Natural Science and Engineering Research Council (NSERC) of Canada. One of us (D.V.) wishes to acknowledge financial support from NSERC and from the University of Toronto.

[1]Th. Fauster, F. J. Himpsel, J. J. Donelon, and A. Marx, Rev. Sci. Instrum. **54**, 68 (1983).

[2]M. J. G. Lee, Phys. Rev. Lett. **36**, 1193 (1973); R. Reifenberger, H. A. Goldberg, and M. J. G. Lee, Surf. Sci. **83**, 599 (1979).

[3]D. L. Haavig and R. Reifenberger, Surf. Sci. **151**, 128 (1985).

[4]D. Venus and M. J. G. Lee, Phys. Rev. B **28**, 437 (1983).

[5]Y. Gao and R. Reifenberger (unpublished).

[6]E. W. Plummer and J. W. Gadzuk, Phys. Rev. Lett. **25**, 1439

(1970).
[7]E. W. Plummer and A. E. Bell, J. Vac. Sci. Technol. **9**, 583 (1972).
[8]R. D. Young and C. E. Kuyatt, Rev. Sci. Instrum. **39**, 1477 (1968).
[9]D. Venus and M. J. G. Lee, Surf. Sci. **125**, 452 (1982).
[10]A. Bagchi, Phys. Rev. B **10**, 542 (1974).
[11]E. L. Murphy and R. H. Good, Jr., Phys. Rev. **102**, 1464 (1956).
[12]A. Modinos, Surf. Sci. **70**, 528 (1978), and references therein.
[13]W. L. Schaich and N. W. Ashcroft, Phys. Rev. B **3**, 2452 (1971).
[14]D. Venus, Ph.D. thesis, University of Toronto, 1985 (unpublished).
[15]E. W. Plummer, in *Interactions on Metal Surfaces,* edited by R. Gomer (Springer-Verlag, New York, 1975).
[16]K. L. Kliewer, in *Photoemission and the Electronic Properties of Surfaces,* edited by B. Feuerbacher, B. Fitton, and R. Willis (Wiley, New York, 1978), p. 45.
[17]P. J. Feibelman, Phys. Rev. B **12**, 1319 (1975).
[18]M. Born and E. Wolf, *Principles in Optics* (Pergamon, Toronto, 1975), p. 633.
[19]E. Taranko, J. Phys. (Paris) **38**, 163 (1977).
[20]S. Doniach, Phys. Rev. B **2**, 3898 (1970).
[21]R. D. Young, Phys. Rev. **113**, 110 (1958).
[22]This is also true if the surface photoeffect is considered. See Ref. 10 and C. Schwartz and M. W. Cole, Surf. Sci. **115**, 290 (1982).
[23]D. Venus and M. J. G. Lee, Rev. Sci. Instrum. **56**, 1206 (1985).
[24]P. J. Donders and M. J. G. Lee, Surf. Sci. **167**, 141 (1986).
[25]D. Venus and M. J. G. Lee, Surf. Sci. **172**, 477 (1986).
[26]L. W. Swanson and L. C. Crouser, Phys. Rev. Lett. **15**, 389 (1966); **19**, 1179 (1967).
[27]S. L. Weng, E. W. Plummer, and T. Gustafsson, Phys. Rev. B **18**, 1718 (1978).
[28]N. E. Christensen and B. Feuerbacher, Phys. Rev. B **10**, 2349 (1974).
[29]B. Feuerbacher and N. E. Christensen, Phys. Rev. B **10**, 2373 (1974).
[30]F. J. Himpsel, Adv. Phys. **32**, 1 (1983).
[31]E. A. Stern, Phys. Rev. B **10**, 3027 (1974).
[32]W. E. Spicer, Phys. Rev. Lett. **11**, 243 (1963).
[33]G. Jezequel, A. Barski, P. Steiner, F. Solal, P. Roubin, R. Pinchaux, and Y. Petroff, Phys. Rev. B **30**, 4833 (1984).
[34]G. Borstel, M. Neumann, and M. Wöhlecke, Phys. Rev. B **23**, 3121 (1981).
[35]A. Messiah, *Quantum Mechanics* (Wiley, New York, 1976), Vol. II, pp. 523 and 731.
[36]P. J. Donders and M. J. G. Lee, Surf. Sci. (to be published).
[37]J. E. Inglesfield, Surf. Sci. **76**, 355 (1978).
[38]T. Radoń, Surf. Sci. **100**, 353 (1980).
[39]T. Radoń and Ch. Kleint, Surf. Sci. **60**, 540 (1976).
[40]H. F. Liu and T. T. Tsong, Rev. Sci. Instrum. **55**, 1779 (1984).
[41]P. J. Donders and M. J. G. Lee (unpublished).
[42]V. Dose, Prog. Surf. Sci. **13**, 225 (1983).
[43]P. O. Nilsson and C. G. Larsson, Jpn. J. Appl. Sci. **17**, Suppl. **17-2**, 144 (1978).
[44]P. O. Nilsson and A. Kovacs, Phys. Scr. **T4**, 61 (1983).
[45]J. B. Pendry, *Low Energy Electron Diffraction* (Academic, London, 1974).
[46]J. B. Pendry, Surf. Sci. **57**, 679 (1976).